Drag Reduction for Supercritical Aerofoils

A. Sedaghat, S. Shahpar, I. M. Hall

The Manchester School of Engineering
Aerospace Engineering Division, Oxford Road
Manchester M13 9PL
UK

Abstract

The aerodynamic performance of supercritical aerofoils at transonic speeds is strongly influenced by the shock wave-boundary layer interaction. As a means of controlling this interaction it has been suggested that the upper part of aerofoil surface, in the shock wave region, is replaced by a porous surface. Quite small suction through the porous surface may cause a significant reduction in the undesirable effects of a strong interaction. The suction effect downstream of the shock wave limits the boundary layer growth and minimizes flow separation.

The main aim of this study is to estimate the reduction in both skin friction and pressure drag produced by small amount of suction or blowing utilizing a modern high resolution numerical scheme. A fast and robust algorithm utilizing an upwind implicit Total Variation Diminishing (TVD) scheme[1] has been used to study both laminar and turbulent transonic flows over the aerofoils with porous surfaces. A hyperbolic C-mesh has been used to generate an orthogonal grid around aerofoil section.

The numerical results obtained for the RAE 2822 aerofoil are compared with experimental data and other numerical results. The results consist of both laminar and turbulent viscous flows over the aerofoils with and without suction.

1. Introduction

In order to reduce undesired effects of shock-boundary layer interaction for supercritical aerofoils, many different techniques have been used. The most attractive method is passive control of shock-boundary layer interaction using a porous surface above a closed plenum chamber underneath the shock wave region. A comprehensive review on theoretical and experimental investigations of passive control was given by Raghunathan[2]. In that review, he concluded that for practical aerofoils the passive control can reduce drag only at off-design condition when shock wave becomes stronger. But, drag reduction at cruise condition is more desirable than off-design condition for transonic civil aircrafts.

In this study, it was decided to maintain laminar flow for whole aerofoil chord length and investigate (computationally) what percentage drag reduction can be achieved at transonic speeds. Experimental investigation at NASA[3] proved that full chord length laminar flow can be obtained by suction through strips. At this stage, we consider the shock-boundary layer interaction to be controlled by a certain amount of air suction through porous surface in the shock wave region.

An implicit TVD scheme has been selected for this study. The TVD concept first proposed by Harten[4,5] and then modified and generalized by Yee[6,7,8] who had implemented to solve the two-dimensional Euler equations of gas-dynamics for aerofoil problems. In most of these papers inviscid aerofoil flows have been considered and the interest is in general flow features such as shock capturing. However, in our study we aim to make the scheme a practical tool for computation of transonic flows over aerofoils and examine the ability of the scheme to accurately predict aerodynamics coefficients. The aerodynamics coefficients which are important from practical point of view can not be resolved efficiently by the original Yee's scheme because of many involved control parameters such as type of limiters, local time-stepping, and dissipation correction at boundaries. Therefore, some modification of the original scheme is introduced[9] to obtain more accurate results.

In the present study, the finite-difference explicit part of flux computation in the Yee's implicit scheme has been replaced by a cell-vertex finite-volume scheme and the implicit part and TVD dissipation functions are also modified. Since at steady-state, the solution of implicit schemes converge to explicit part by vanishing the implicit part, we can claim that the final results are truely based on a finite-volume scheme which is mostly desirable for aerofoil flows. The derivation of

Copyright © 1996 by the AIAA and ICAS. All rights reserved.

this class of TVD schemes in two-dimensional generalized curvilinear coordinates and details of the scheme can be found in references[9,10,11] for solving compressible flows. Details of the Baldwin-Lomax[12] turbulent model in non-dimensional form used here is explained and the numerical implementation of this turbulent model is discussed.

The goal is to assess the performance of this scheme in terms of numerical accuracy, robustness and convergence rate for drag reduction purposes. The RAE 2822 aerofoil is selected as a test case to compare laminar and turbulent numerical results on a relatively coarse grid. The 24 % drag reduction obtained for RAE 2822 (case 10) is a very promising result at this stage and we are now aiming to include all physical phenomena such as controlling the transition of laminar flow to turbulent in the future investigation.

2. Governing Equations

The nondimensional form of the compressible Navier-Stokes equations in the general curvilinear coordinates in two dimension can be written as

$$\frac{\partial \hat{\mathbf{U}}}{\partial t} + \frac{\partial \hat{\mathbf{F}}}{\partial \xi} + \frac{\partial \hat{\mathbf{G}}}{\partial \eta} = 0 \qquad (1)$$

where

$$\begin{aligned} \hat{\mathbf{U}} &= \mathbf{U}/J \\ \hat{\mathbf{F}} &= (\xi_x \mathbf{F} + \xi_y \mathbf{G})/J \quad , \quad \hat{\mathbf{G}} = (\eta_x \mathbf{F} + \eta_y \mathbf{G})/J \\ J &= \xi_x \eta_y - \xi_y \eta_x \end{aligned} \qquad (2)$$

$\xi = \xi(x,y), \eta = \eta(x,y)$ are coordinate transformation functions and J is the Jacobian of the transformation. The vectors $\mathbf{U}$, $\mathbf{F}$, and $\mathbf{G}$ are given by

$$\mathbf{U} = \begin{bmatrix} \rho \\ \rho u \\ \rho v \\ e \end{bmatrix}$$

$$\mathbf{F} = \begin{bmatrix} \rho u \\ p + \rho u^2 - \tau_{xx} \\ \rho uv - \tau_{xy} \\ (e+p)u - u\tau_{xx} - v\tau_{xy} + q_x \end{bmatrix}$$

$$\mathbf{G} = \begin{bmatrix} \rho v \\ \rho uv - \tau_{xy} \\ p + \rho v^2 - \tau_{yy} \\ (e+p)v - u\tau_{xy} - v\tau_{yy} + q_y \end{bmatrix} \qquad (3)$$

where ρ, u, v, p and e are the density, velocity components along the x_- and y_- directions, static pressure and total energy respectively. The components of the shear-stress tensor and the heat flux vector in non-dimensional form are given by

$$\begin{aligned} \tau_{xx} &= \frac{\mu}{Re}\left(\frac{4}{3}\frac{\partial u}{\partial x} - \frac{2}{3}\frac{\partial v}{\partial y}\right) \\ \tau_{yy} &= \frac{\mu}{Re}\left(\frac{4}{3}\frac{\partial v}{\partial y} - \frac{2}{3}\frac{\partial u}{\partial x}\right) \\ \tau_{xx} &= \frac{\mu}{Re}\left(\frac{\partial u}{\partial y} + \frac{\partial v}{\partial x}\right) \\ q_x &= \frac{-\mu\,\gamma}{(\gamma-1)\,Re\,Pr}\frac{\partial (p/\rho)}{\partial x} \\ q_y &= \frac{-\mu\,\gamma}{(\gamma-1)\,Re\,Pr}\frac{\partial (p/\rho)}{\partial y} \end{aligned} \qquad (4)$$

where μ, γ, Pr and Re are the dynamic viscosity, ratio of specific heats, the Prandtl number, and the Reynolds number based on the chord length.

The following non-dimensionalization are used to write the governing fluid flow equations, and all subsequent equations, are in non-dimensional form.

$$x = \frac{x^*}{c} \;,\; y = \frac{y^*}{c} \;,\; u = \frac{u^*}{U_\infty} \;,\; v = \frac{v^*}{U_\infty} \;,\; t = \frac{t}{c/U_\infty}$$

$$\rho = \frac{\rho^*}{\rho_\infty} \quad , \quad T = \frac{T^*}{T_\infty} \quad , \quad p = \frac{p/p_\infty}{\gamma M_\infty^2}$$

$$\mu_l = \frac{\mu_l^*}{\mu_{\infty_l}} \quad , \quad \mu_t = \frac{\mu_t^*}{\mu_{\infty_l}} \quad , \quad \tau_w = \frac{\tau_w^*}{\rho_\infty\, U_\infty^2}$$

where c, ρ_∞, p_∞, and U_∞ are chord length and free-stream density, pressure and velocity, respectively. The Mach number is $M_\infty = U_\infty/C_\infty$ with the free-stream sound speed C_∞.

3. The Numerical Algorithm

The Alternative Direction Implicit (ADI) form of Linearized Conservative Implicit (LCI) TVD scheme in generalized curvilinear coordinates can be written as[6,11]

$$\begin{aligned} \{\mathbf{I} + \Delta t_{ij}\,(\mathbf{H}^{\xi}_{i+1/2,j} - \mathbf{H}^{\xi}_{i-1/2,j})\}\frac{\mathbf{E}^*}{J} &= \frac{\mathbf{RHS}}{J} \\ \{\mathbf{I} + \Delta t_{ij}\,(\mathbf{H}^{\eta}_{i,j+1/2} - \mathbf{H}^{\eta}_{i,j-1/2})\}\frac{\mathbf{E}^n}{J} &= \frac{\mathbf{E}^*}{J} \end{aligned} \qquad (5)$$

with $\mathbf{U}^{n+1} = \mathbf{U}^n + \mathbf{E}^n$. The operatores $\mathbf{H}^{\xi}$ and $\mathbf{H}^{\eta}$ are defined as

$$\begin{aligned} \mathbf{H}^{\xi}_{i\pm1/2,j}\mathbf{E}^* &= \frac{1}{2}[\hat{\mathbf{A}}_{i\pm1,j}\mathbf{E}^*_{i\pm1,j} - \mathbf{\Omega}^{\xi}_{i\pm1/2,j}\mathbf{E}^*] \\ \mathbf{H}^{\eta}_{i,j\pm1/2}\mathbf{E}^n &= \frac{1}{2}[\hat{\mathbf{B}}_{i,j\pm1}\mathbf{E}^n_{i,j\pm1} - \mathbf{\Omega}^{\eta}_{i,j\pm1/2}\mathbf{E}^n] \end{aligned} \qquad (6)$$

The Jacobian matrices $\hat{\mathbf{A}}$ and $\hat{\mathbf{B}}$ result from the linearization of the flux vectors $\hat{\mathbf{F}}$ and $\hat{\mathbf{G}}$ respectively. For steady-state applications

$$\begin{aligned} \mathbf{\Omega}^{\xi}_{i+1/2,j}\mathbf{E}^* &= M^{\xi}_{i+1/2,j}\mathbf{I}(\mathbf{E}^*_{i+1,j} - \mathbf{E}^*_{i,j}) \\ \mathbf{\Omega}^{\eta}_{i,j+1/2}\mathbf{E}^n &= M^{\eta}_{i,j+1/2}\mathbf{I}(\mathbf{E}^n_{i,j+1} - \mathbf{E}^n_{i,j}) \end{aligned} \qquad (7)$$

The scalar values M^{ξ} and M^{η} are

$$\begin{aligned} M^{\xi}_{i+1/2,j} &= max[\psi(a^l_{i+1/2})] \\ M^{\eta}_{i+1/2,j} &= max[\psi(a^l_{j+1/2})] \end{aligned} \qquad (8)$$

I, $a^l_{i+1/2}$ and $a^l_{j+1/2}$, and ξ are (4×4) identity matrix, the eigenvalues correspond to the $\hat{\mathbf{A}}$ and $\hat{\mathbf{B}}$, and entropy correction function, respectively. The **RHS** here is a combination of a cell-vertex finite-volume[13] approach and the numerical dissipation of the Yee's TVD scheme as:

$$\begin{aligned}\mathbf{RHS} &= -\frac{\Delta t_{i,j}}{A_{i,j}}\sum_{AB}^{DA}(\mathbf{F}\Delta y - \mathbf{G}\Delta x) \\ &- \frac{\Delta t_{i,j}}{2}[(\mathbf{R}_{i+1/2,j}\mathbf{\Phi}_{i+1/2,j} - \mathbf{R}_{i-1/2,j}\mathbf{\Phi}_{i-1/2,j}) \\ &+ (\mathbf{R}_{i,j+1/2}\mathbf{\Phi}_{i,j+1/2} - \mathbf{R}_{i,j-1/2}\mathbf{\Phi}_{i,j-1/2})] \quad (9)\end{aligned}$$

$(\phi^l_{i+1/2})^U$ for the second-order upwind TVD scheme[9,10], are given by

$$\begin{aligned}(\phi^l_{i+1/2})^U &= \frac{1}{2}\psi(a^l_{i+1/2})(g^l_{i+1} + g^l_i) \\ &- \psi(a^l_{i+1/2} + \gamma^l_{i+1/2})\alpha^l_{i+1/2} \quad (10)\end{aligned}$$

with the functions γ and ψ defined as

$$\gamma^l_{i+1/2} = \frac{1}{2}\psi(a^l_{i+1/2})\begin{cases}(g^l_{i+1} - g^l_i)/\alpha^l_{i+1/2} & \alpha^l_{i+1/2} \neq 0 \\ 0 & \alpha^l_{i+1/2} = 0\end{cases} \quad (11)$$

$$\psi(z) = \begin{cases}|z| & |z| \geq \epsilon \\ (z^2 + \epsilon^2)/2\epsilon & |z| < \epsilon\end{cases} \quad (12)$$

with $\epsilon = 0.125$. The characteristic function $\alpha^l_{i+1/2}$ is defined as

$$\alpha^l_{i+1/2} = \mathbf{R}^{-1}_{i+1/2}(\mathbf{U}_{i+1} - \mathbf{U}_i) \quad (13)$$

with $\mathbf{R}$ is right eigen-vector matrix.
In all test cases, the Van-Leer limiter functions $g^l_{i+1/2}$ is used and is given by[1,9]

$$\begin{aligned}g^l_i &= \{\alpha^l_{i-1/2}[(\alpha^l_{i+1/2})^2 + \delta] + \alpha^l_{i+1/2}[(\alpha^l_{i-1/2})^2 + \delta]\} \\ &/[(\alpha^l_{i+1/2})^2 + (\alpha^l_{i-1/2})^2 + 2\delta] \quad (14)\end{aligned}$$

with δ a small parameter $(10^{-7} \leq \delta \leq 10^{-5})$. In all the above equations the Roe's averaging[14] is used to evaluate $\mathbf{U}_{i+1/2}$ and corresponding terms.

4. The Turbulent Model

For laminar flow computation the coefficient of molecular viscosity μ_l is obtained from Sutherland's law expressed by

$$\mu_l = T^{3/2}\frac{1.0 + C/T_\infty}{T + C/T_\infty} \quad (15)$$

with $C = 110.4K$ and the coefficient of thermal conductivity κ is specified by

$$\frac{\kappa_l}{c_p} = \frac{\mu_l}{Pr_l}$$

where the laminar Prandtl number Pr_l is a constant equals to 0.72 for air.

For turbulent flow computations, using a zero-equation model, the transport coefficients in Navier-Stokes equations are simply replaced by

$$\begin{aligned}\mu &= \mu_l + \mu_t \\ \frac{\kappa}{c_p} &= \frac{\mu_l}{Pr_l} + \frac{\mu_t}{Pr_t}\end{aligned} \quad (16)$$

where the turbulent Prandtl number used here is a constant equals to 0.9 for air and the turbulent viscosity coefficient μ_t is computed using the isotropic, two-layer, Cebeci-type, algebraic eddy-viscosity model reported by Baldwin and Lomax[12].

In the Baldwin-Lomax two-layer formulation μ_t is given by:

$$\mu_t = \begin{cases}(\mu_t)_{inner} & , \quad y \leq y_c \\ (\mu_t)_{outer} & , \quad y > y_c\end{cases} \quad (17)$$

where y is the local distance measured normal to the body surface and y_c is the smallest value of y at which the values from the inner and outer region formulas are equal. In practice y_c corresponds to the y at which $(\mu_t)_{inner} \geq (\mu_t)_{outer}$. Within the inner region

$$(\mu_t)_{inner} = Re_\infty.\rho.l^2_m(y).\mid \omega \mid \quad (18)$$

where ω is the vorticity defined by

$$\omega = \frac{\partial u}{\partial y} - \frac{\partial v}{\partial x} \quad (19)$$

and l_m is the mixing length expressed as

$$l_m(y) = Ky[1 - exp(-y^+/A^+] \quad (20)$$

y is the surface normal distance, and y^+ is defined as

$$y^+ = Re_\infty\frac{\sqrt{\rho_w\tau_w}}{\mu_w}y \quad (21)$$

τ_w is the wall shear stress and given by

$$\tau_w = \frac{1.0}{Re_\infty}\mu_w\left(\frac{\partial u_t}{\partial y}\right)_w \quad (22)$$

u_t is the mean-velocity component tangential to the surface.

The outer region formulation is given by

$$(\mu_t)_{outer} = Re_\infty.C_{cs}.C_{cp}.\rho.F_{wake}/F_{kleb} \quad (23)$$

where F_{wake} is the maximum value of the function

$$F(y) = \frac{l_m(y)}{K}\mid \omega \mid \quad (24)$$

F_{kleb} is the Klebanoff intermittency factor defined as

$$F_{kleb} = \left[1.0 + 5.5\left(\frac{C_{kleb}\ y}{y_{max}}\right)^6\right] \quad (25)$$

y_{max} being the value of y for F_{max}. To determine each peak in F, it is suggested by Degani[15] that the value $F_{peak} = F(y_{peak})$ is chosen when $F(y) < 0.9F(y_{peak})$ for $y > y_{peak}$.
The turbulent model involves the following five constants:

$$K = 0.41 \quad , \quad A^+ = 26 \quad , \quad C_{cs} = 0.0168$$

$$C_{cp} = 1.6 \quad , \quad C_{kleb} = 0.3$$

For practical implementation in a CFD code, the term y_{max}, which involves a search across the boundary layer at each station, must be determined to find the position of F_{max}, the maximum value of the function F in Equation (24). The length scale y_{max} is used as a characteristic scale for the outer part of the boundary layer, and so near wall peaks in F must be ignored. This is accomplished by restricting the search for F_{max} to $y^+ > 10$. Secondly, multiple peaks in F may occure, particularly downstream of shock waves. An effective strategy used in reference[16] is to search across the boundary layer, starting at $y^+ > 10$, for the first three peaks and to take the largest of these peaks to determine y_{max}.

In the wake region a simple wake model is used i.e., the upper and lower surface trailing edge eddy-viscosity distributions are imposed at all stations downstream in the wake

$$\begin{cases} (\mu_t)^U_{wake} = (\mu_t)^U_{t.e.} \\ (\mu_t)^L_{wake} = (\mu_t)^L_{t.e.} \end{cases} \tag{26}$$

As far as the flow development around the aerofoil is considered, the above approximation for the immediate near-wake region gives a reasonable estimation.

5. Results and Discussion

Results are presented in this section of calculation of the RAE 2822 covering a range of conditions from fully subcritical flow to supercritical flow with shock-induced separation. The calculations are made using the method with a fixed set of flow algorithm and grid generation parameters.

Computational grids are constructed using the algebraic grid generator of Rizzi[17] together with a hyperbolic grid generator of Alsalihi[18] to produce an orthogonal C-mesh for the test cases (see Fig. 1). A relatively coarse mesh of 141 × 61 has been used in order to investigate performance of the numerical results. The outer boundary is placed at 18 chord lengths away from the aerofoil surface. The first cell-size at both the leading edge and the trailing edge is fixed to $\frac{\Delta\xi}{c} = 0.002$ and $\frac{\Delta\eta}{c} = 0.00002$. In the wake region 24 × 61 grid points have been placed between the upper and the lower wake cut and the outflow boundary which is placed 10 chords length downstream of the trailing edge.

Each test case was initialized with a uniform freestream flow at the prescribed Mach number and angle of attack. The no-slip condition together with zero normal pressure gradient and normal temperature gradient (adiabatic wall) have been applied on the aerofoil surface. The characteristic boundary condition[19] has been used for the outer-boundary and zero-extrapolation was used for the outflow boundary. In the wake region simple averaging has been applied to all conservative variables.

A local time-stepping similar to Pulliam and Steger[6] is used here is based on mesh Jacobians as follows

$$\Delta t_{i,j} = \frac{T}{1 + \sqrt{J_{i,j}}} \tag{27}$$

where T is a constant to provide the maximum allowed time-step which can maintain the stability of the numerical scheme. A typical value used in our computation for T is 0.5.

The RAE 2822 aerofoil has been designed for transonic flows and has a maximum thickness/chord ratio of 12.1 % and a sharp trailing edge. An extensive experimental study of this aerofoil in the 8ft × 6ft transonic wind tunnel at RAE Farnborough was presented by Cook et al[20]. It has been used extensively to validate numerical methods[21].

Figure 1 shows the RAE 2822 aerofoil with a close-up of the computational grid used in the present calculation. Four cases are considered here and the relevant flow conditions are given in Table 1(a). Comparisons of predicted and measured lift, drag and pitching moment coefficients and also Johnston's[16] numerical results are shown in Table 1(b), the results being presented for the Baldwin-Lomax turbulence model. Note that Johnston's results are based on a fairly fine mesh consisting of 272 × 64 cells.

Transition is fixed at 11 % chord for Case 1 and at 3 % chord for the others on the upper and lower surfaces of the aerofoil.

Considering the Case 1 which involves mainly subcritical flow, the agreement with measurements is fairly good, especially, drag prediction is very close to experiment. Figure 2 shows that pressure coefficient on upper and lower aerofoil surfaces are fairly matched with results from experiment. The predicted skin friction is generally in good agreement with measurements. Drag convergence is oscillatory due to the relatively large time step is used. However, convergence can be achieved in around 3000 iterations for engineering applications.

TABLE 1
RAE 2822 Aerofoil
Results using Baldwin-Lomax (B-L) model
(a) Flow conditions

Case	M	α	$R_e \times 10^{-6}$
1	0.676	1.93^o	5.7
6	0.725	2.54^o	6.5
9	0.730	2.79^o	6.5
10	0.750	2.81^o	6.2

b) Comparison of measured and calculated loads

Case 1	C_L	C_D	$C_M(1/4)$
Experiment	0.566	0.0085	-0.082
Johnston (B-L)	0.5802	0.01068	-0.08769
present (B-L)	0.5750	0.0084	-0.08593

Case 6	C_L	C_D	$C_M(1/4)$
Experiment	0.743	0.0127	-0.095
Johnston (B-L)	0.7457	0.01502	-0.09175
present (B-L)	0.7637	0.01199	-0.09255

Case 9	C_L	C_D	$C_M(1/4)$
Experiment	0.803	0.0168	-0.099
Johnston (B-L)	0.7950	0.01884	-0.09513
present (B-L)	0.8174	0.01593	-0.09642

Case 10	C_L	C_D	$C_M(1/4)$
Experiment	0.743	0.0242	-0.106
Johnston (B-L)	0.7901	0.02921	-0.1108
present (B-L)	0.8157	0.02582	-0.1117

Case 6 presents a supercritical flow on the upper surface terminated by a shock wave of moderate strength just downstream of the mid-chord position. Drag and moment coefficients predicted by present method are in good agreement with measurements. However, the predicted lift coefficient is a little higher than the other numerical scheme and measurement. Similarly, as shown in Figure 3, the shock wave is predicted to be a little too far upstream. This is in agreement with other calculation methods; see Johnston[16], and Holst[21] for example. Very good agreement in skin friction is achieved upstream of the shock wave, but, relatively poor prediction is observed downstream of the shock wave which results from the discrepancies in shock wave position. Rapid and robust convergence of drag coefficient is found.

Most aerodynamics coefficients are matched closely with the measurements for Case 9. In Figure 4 , better agreement in shock wave position is observed as also reported by Johnston. The upper surface skin friction distribution, in Figure 4(b), indicates flow separation at the foot of the shock wave for the Baldwin-Lomax turbulent model. No separation in the experiment is reported for this case[20]. This tendency of the Baldwin-Lomax model to predict premature flow separation, particularly at shock waves, has been noted by other authors[21]. Similar convergence with the other test cases is observed.

Case 10 is the most interesting of the RAE 2822 cases to be considered, since it is the only one in which shock-induced separation is present in the experiment. Figure 5 shows that there are now larger discrepancies between prediction and measurements. The flow remains separated up to the trailing edge for the Baldwin-Lomax turbulent model. This behavior has been related to the use of the friction velocity U_τ in the near-wall damping function by Johnston[16].

Figure 6 shows the results obtained for RAE 2822 aerofoil with and without suction underneath the shock wave. The case 10 is selected here to investigate the effects of suction on flow separation. For the porous aerofoil, suction equivalent to 1% of freestream velocity is employed along the segment of $0.6 < x_{i,1} < 0.8$ on the upper part of aerofoil surface. 24% drag reduction is achieved, which is very promising for future investigation. However, all physical flow features such as transition from laminar to turbulent flow, have to be considered to accurately resolve all physical phenomena.

To see all the merits of maintaining laminar flow on supercritical aerofoils in respect to drag reduction, the laminar fluid flow equations have been solved and results are compared with turbulent results. Figure 6(a) shows that the shock wave for the porous aerofoil moves slightly downstream with respect to solid aerofoil result. The suction upstream of the shock wave causes the shock wave to become stronger and the flow tends to separate. However, immediate suction downstream of the shock wave prevents the flow separation and causes a rapid reattachment. Using the appropriate amount of suction, however, will prevent the occurance of any local separation. The laminar flow result has also predicted the wrong shock wave position and this may suggest that more study of laminar flows are needed before involving more complicated turbulence models.

6. Conclusion

In the initial phase of this study, a fast algorithm utilizing an upwind, implicit, Total Variation Diminishing (TVD) scheme has been developed. Both laminar and turbulent transonic flows over aerofoils with and without porous surfaces have been studied. A hyperbolic C-mesh has been used to provide an orthogonal grid around the aerofoil section. This study has shown that aerodynamic coefficients can be predicted fairly accurately using a relatively coarse orthogonal grid. The current study of laminar transonic flows has indicated that active laminar flow control (LFC) can also be in-

vestigated by such a method and any possible drag reduction can be analyzed in detail. This is the subject of current research.

References

(1) Yee, H. C., Warming R. F. and Harten A., "Implicit Total Variation Diminishing (TVD) Schemes for Steady-State Calculations", *J. Comp. Phys.*, 57, pp. 327-360, 1985.

(2) Raghunathan, S., "Passive Control of Shock-Boundary Layer Interaction", *Prog. Aerospace Sci.*, Vol. 25, pp. 271-296, 1988.

(3) Harris, C. D., et. al., "The NASA Langley Laminar-Flow-Control Experiment on Swept Supercritical Airfoil", NASA TM 4100, June 1989.

(4) Harten A., "On a Class of High Resolution Total-Variation Stable Finite-Difference Schemes," *NYU Report*, Oct. 1982; *SIAM J. Num. Analysis*, Vol. 21, pp. 1-23, 1983.

(5) Harten A., "A High Resolution Scheme for the Computation of Weak Solutions of Hyperbolic Conservation Laws," *J. Comp. Phys.* , 49, pp. 357-393, 1983.

(6) Yee, H. C. and Harten A., "Implicit TVD Schemes for Hyperbolic Conservation Laws in Curvilinear Coordinates," *AIAA J.*, Vol. 25, No. 2, pp. 226-274, 1986.

(7) Yee, H. C., "Numerical Experiments with a Symmetric High-Resolution Shock- Capturing Scheme," *Procceding of Tenth International Conference on Numerical Methods in Fluid Dynamics*, Lecture Notes in Physics 264, Beijing, China, 1986.

(8) Yee, H. C., "Linearized Form of Implicit TVD Schemes for the Multidimensional Euler and Navier-Stokes Equations," *Advances in Hyperbolic Partial Differential Equations, International Journal on Computers and Mathematics with Applications*, Vol. 12 A, Nos. 4/5, pp. 413-432, 1986.

(9) Sedaghat, A, "Comparative Study of High-Resolution Shock-Capturing Schemes for External Supersonic Flows", *MSc thesis*, Manchester University, 1993.

(10) Montagne, J. L. and Yee, H. C., "Comparative Study of High-Resolution Shock-Capturing Schemes for a Real Gas," *AIAA J.*, Vol. 27, No. 10, pp. 1332-1346, 1988.

(11) Yee, H. C., Klopfer, G. H. and Montagne, J. L. "High-Resolution Shock-Capturing Schemes for Inviscid and Viscous Hypersonic Flows," *NASA TM-100097*, April 1988.

(12) Baldwin, B. and Lomax, H., "Thin Layer Approximation and Algebraic Model for Separated Turbulent Flows," *AIAA Paper No. 78-257*, 1978.

(13) Fletcher, C. A. J., "Computational Techniques for Fluid Dynamics," *Springer-Verlag*, 1988.

(14) Roe, P. L., "Approximate Riemann Solvers, Parameter Vectors, and Difference Schemes," *J. Comp. Phys.*, Vol. 43, pp. 357-372, 1981.

(15) Degani, D. and Schiff, L. B., "Computation of Supersonic Viscous Flows Around Pointed Bodies at Large Incidence," *AIAA Paper No. 83-0034*, 1983.

(16) Johnston, L. J., "Solution of the Reynolds-Averaged Navier-Stokes Equations for Transonic Aerofoil Flows," *Aeronautical J.*, pp. 253-273, 1991.

(17) Rizzi, A. and Vivand H., "Numerical Methods for the Computation of of Inviscid Transonic Flows with Shock Waves," *Notes on Numerical Fluid Mechanics* , Vol 3, Vieweg, 1981.

(18) Alsalihi, Z., "Two Dimensional Hyperbolic Grid Generation," *Von Karman Institute for Fluid Dynamics, Technical Note 162*, October 1987.

(19) Jameson, A. and Baker, T. J., "Solution of the Euler Equations for Complex Configurations," *AIAA Paper No. 83-1929*, 1983.

(20) Cook, P. H., McDonald, M. A., and Firmin, M. C. P., "Aerofoil RAE 2822 - Pressure Distribution, and Boundary Layer and Wake Measurements", *AGARD AR 138*, Paper A6, May 1979.

(21) Holst, T. L., "Viscous Transonic Airfoil Workshop Compendium of Results ," *AIAA Paper No. 87-1460*, 1987; *J. Aircraft*, Vol. 25, No. 12, pp. 1073-1087, 1988.

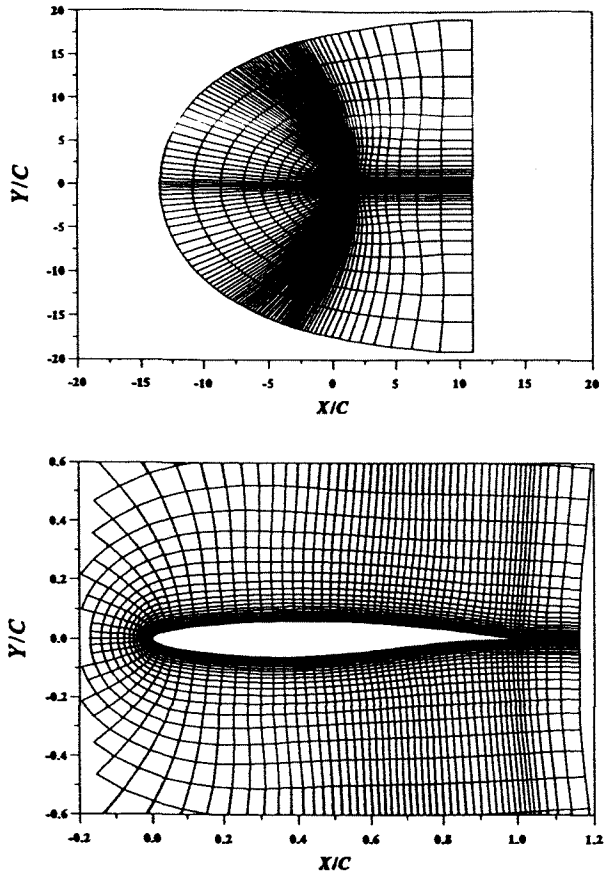

Figure 1 A global and sectional view of the C-hyperbolic mesh generated around the RAE2822 aerofoil.

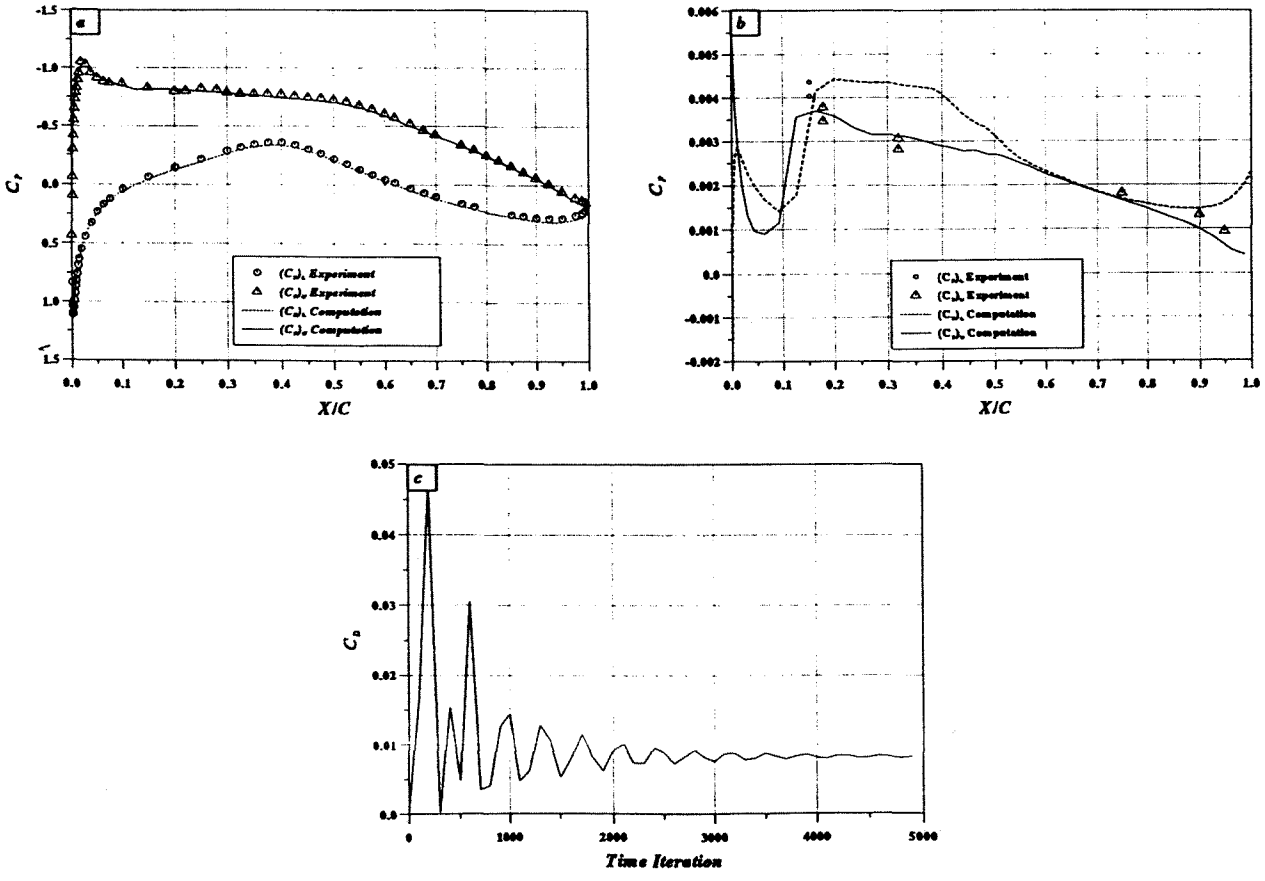

Figure 2 Results for RAE 2822 (case 1), M=0.676, α=1.93°, R_e=5.7 X 10^6
a) surface pressure coefficient; b) surface skin friction; c) drag convergence.

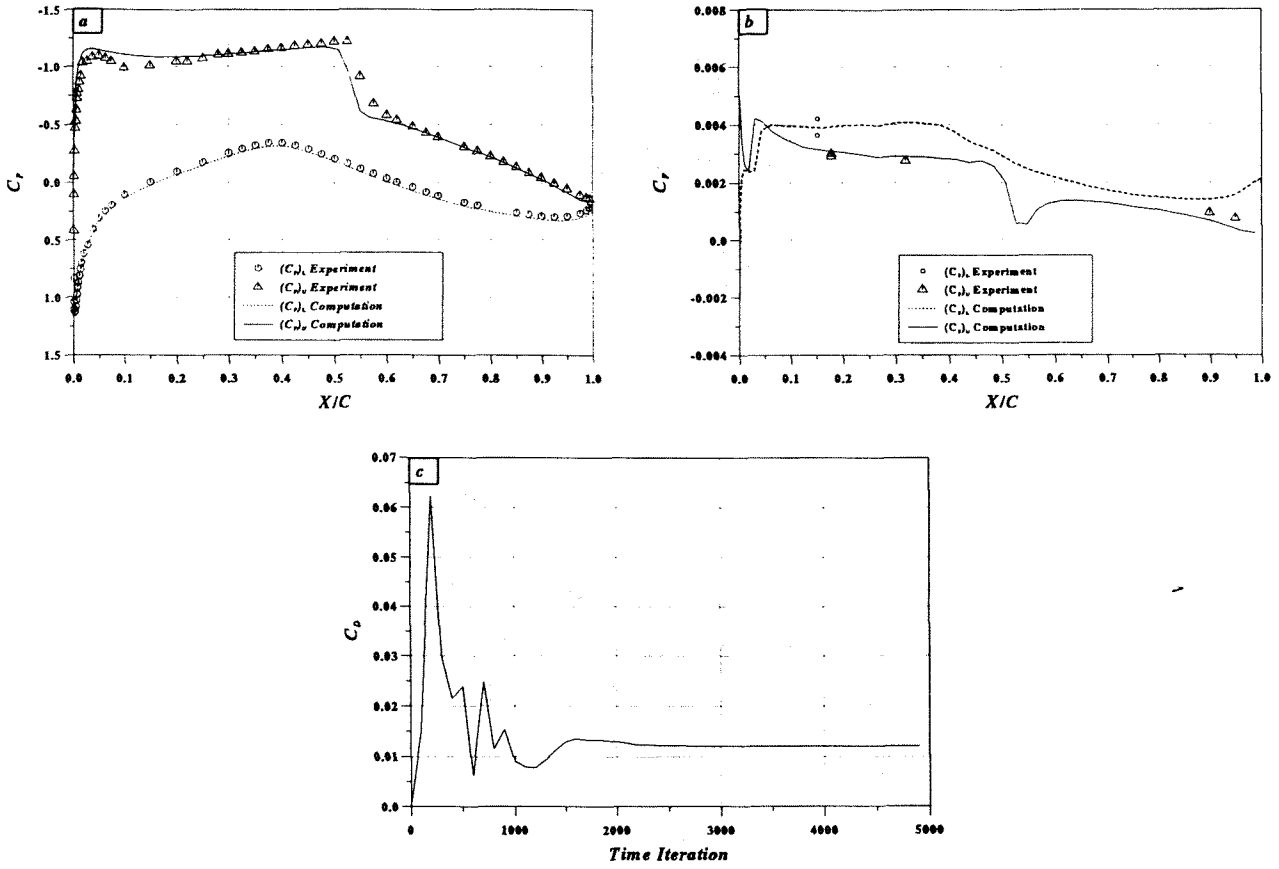

Figure 3 Results for RAE 2822 (case 6), M=0.725, α=2.54°, R_e=6.5 X 10^6
a) surface pressure coefficient; b) surface skin friction; c) drag convergence.

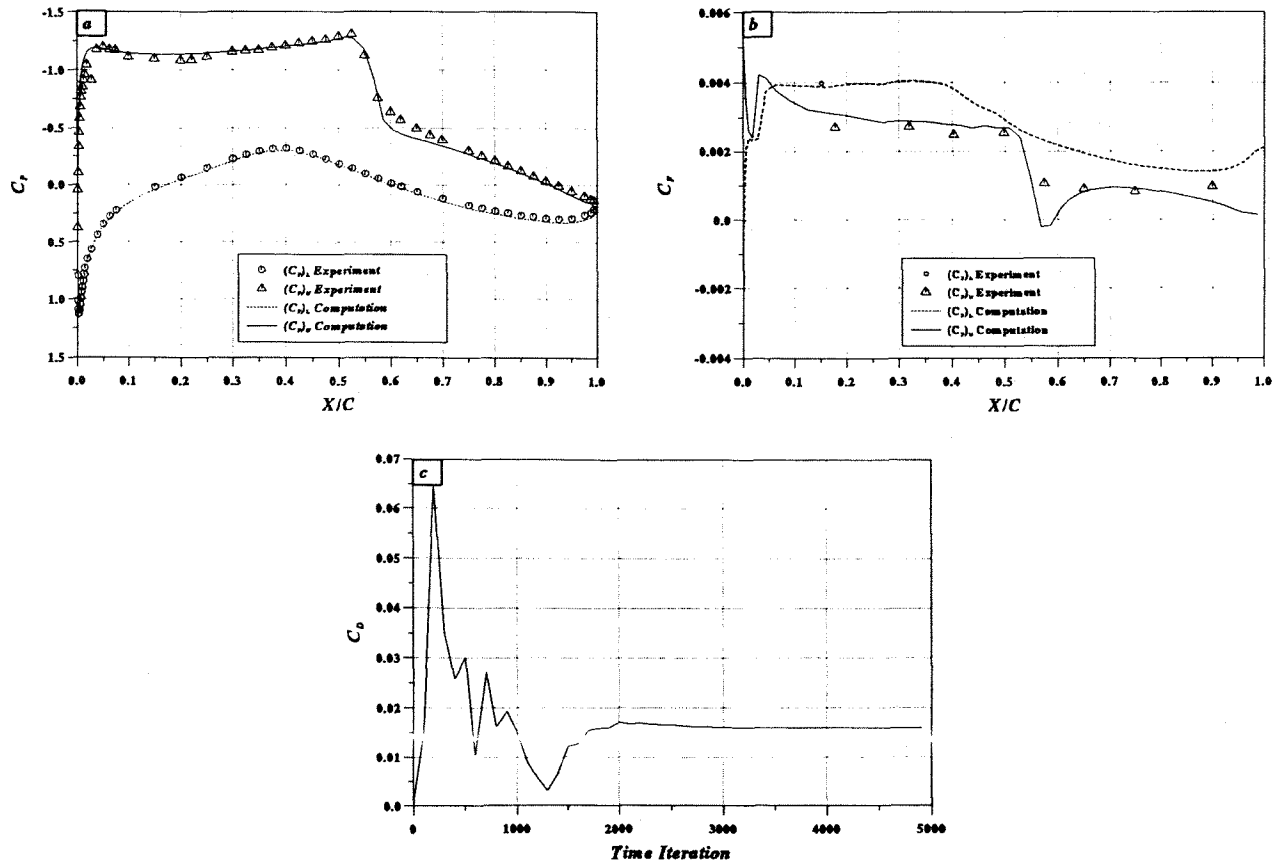

Figure 4 Results for RAE 2822 (case 9), M=0.73, α=2.79°, R_e=6.5 X 10^6
a) surface pressure coefficient; b) surface skin friction; c) drag convergence.

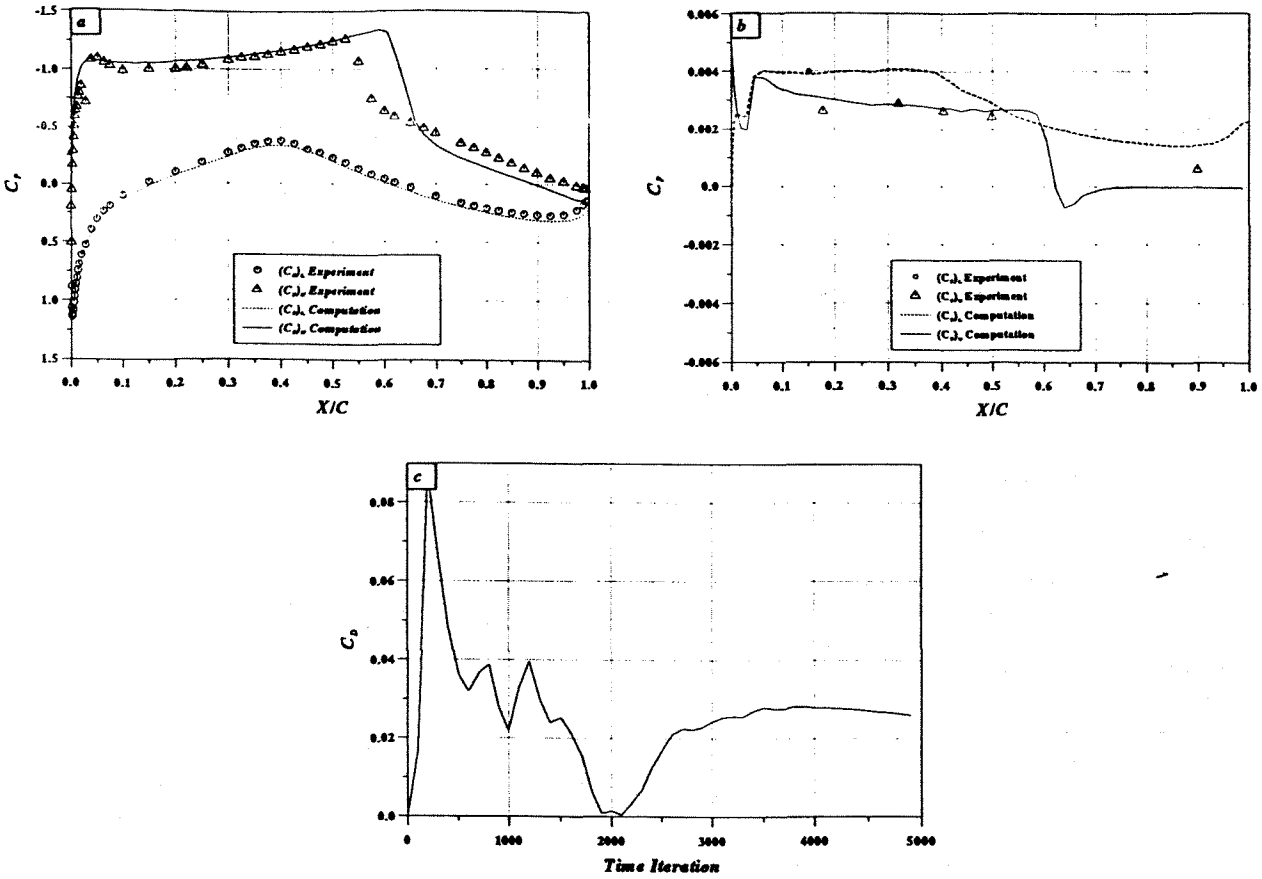

Figure 5 Results for RAE 2822 (case 10), M=0.75, α=2.81°, R_e=6.2 X 10^6
a) surface pressure coefficient; b) surface skin friction; c) drag convergence.

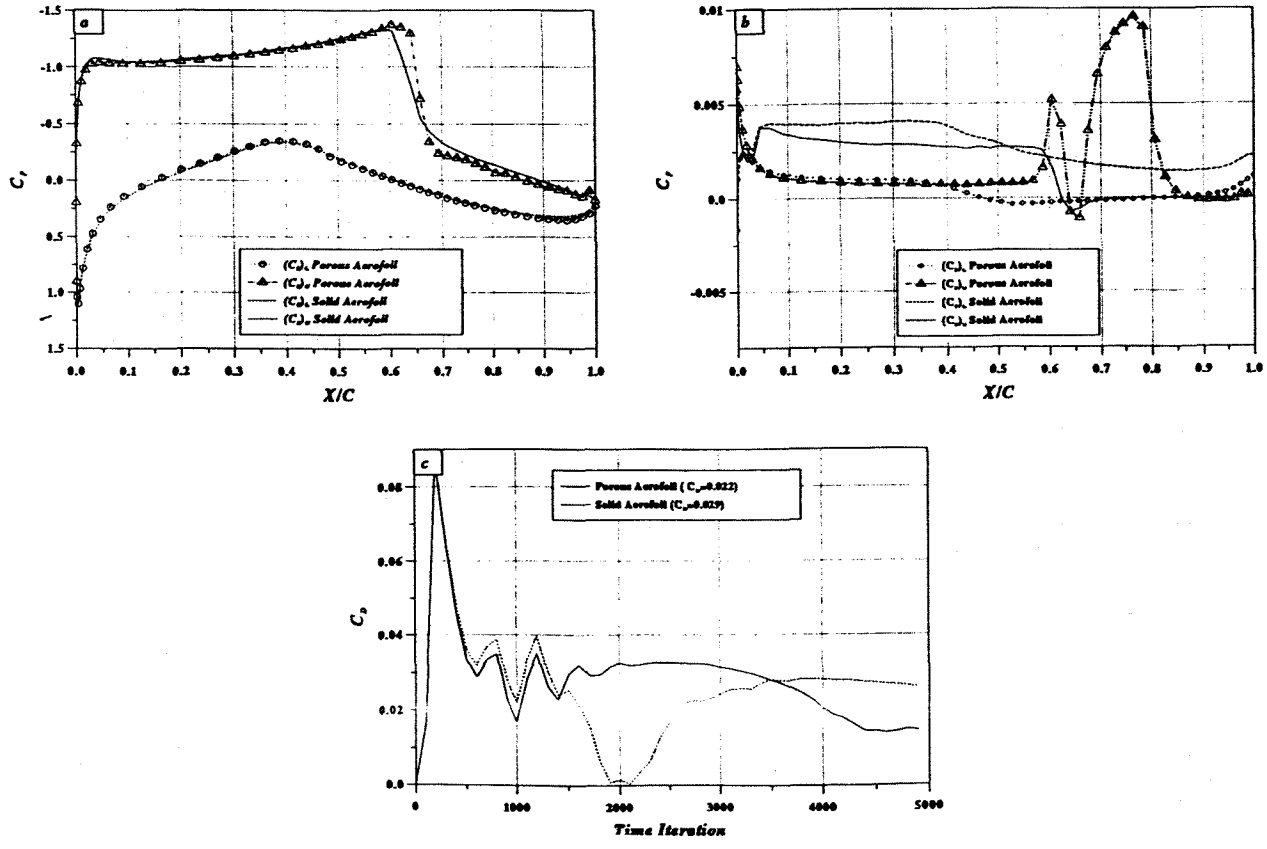

Figure 6 Comparison of solid and porous RAE 2822 Aerofoil (case 10)
a) surface pressure coefficient; b) surface skin friction; c) drag convergence.